

PAPER • OPEN ACCESS

## A scalable helium gas cooling system for trapped-ion applications

To cite this article: F R Lebrun-Gallagher *et al* 2022 *Quantum Sci. Technol.* **7** 024002

View the [article online](#) for updates and enhancements.

You may also like

- [Andreev reflection of massive pseudospin-1 fermions](#)  
Wen Zeng and Rui Shen
- [Effect of V/Fe composite interlayer on the microstructure and mechanical properties of electron beam welded joints of Ta-10W and GH3128](#)  
Yingnan Li, Dong Li and Zhengyi Cao
- [Exploring pathways to deep decarbonization and the associated environmental impact in China's ammonia industry](#)  
Fu Zhao, Ying Fan, Shaohui Zhang et al.



**IOP | ebooks™**

Bringing together innovative digital publishing with leading authors from the global scientific community.

Start exploring the collection—download the first chapter of every title for free.

# Quantum Science and Technology



## PAPER

# A scalable helium gas cooling system for trapped-ion applications

### OPEN ACCESS

RECEIVED  
31 December 2021

REVISED  
1 March 2022

ACCEPTED FOR PUBLICATION  
14 March 2022

PUBLISHED  
29 March 2022

Original content from this work may be used under the terms of the [Creative Commons Attribution 4.0 licence](#).

Any further distribution of this work must maintain attribution to the author(s) and the title of the work, journal citation and DOI.



F R Lebrun-Gallagher<sup>1,2</sup>, N I Johnson<sup>1</sup>, M Akhtar<sup>1,2</sup>, S Weidt<sup>1,2</sup>, D Breaud<sup>1,3</sup>, S J Hile<sup>1</sup>, A Owens<sup>1</sup>, F Bonus<sup>2,4</sup> and W K Hensinger<sup>1,2,\*</sup>

<sup>1</sup> Sussex Centre for Quantum Technologies, University of Sussex, Brighton, BN1 9RH, United Kingdom

<sup>2</sup> Universal Quantum Ltd, Brighton, BN1 6SB, United Kingdom

<sup>3</sup> QOLS, Blackett Laboratory, Imperial College London, London, SW7 2BW, United Kingdom

<sup>4</sup> Department of Physics and Astronomy, University College London, London, WC1E 6BT, United Kingdom

\* Author to whom any correspondence should be addressed.

E-mail: [w.k.hensinger@sussex.ac.uk](mailto:w.k.hensinger@sussex.ac.uk)

**Keywords:** cryogenic ion-trap system, closed-loop cryogenic system, scalable quantum computing architecture

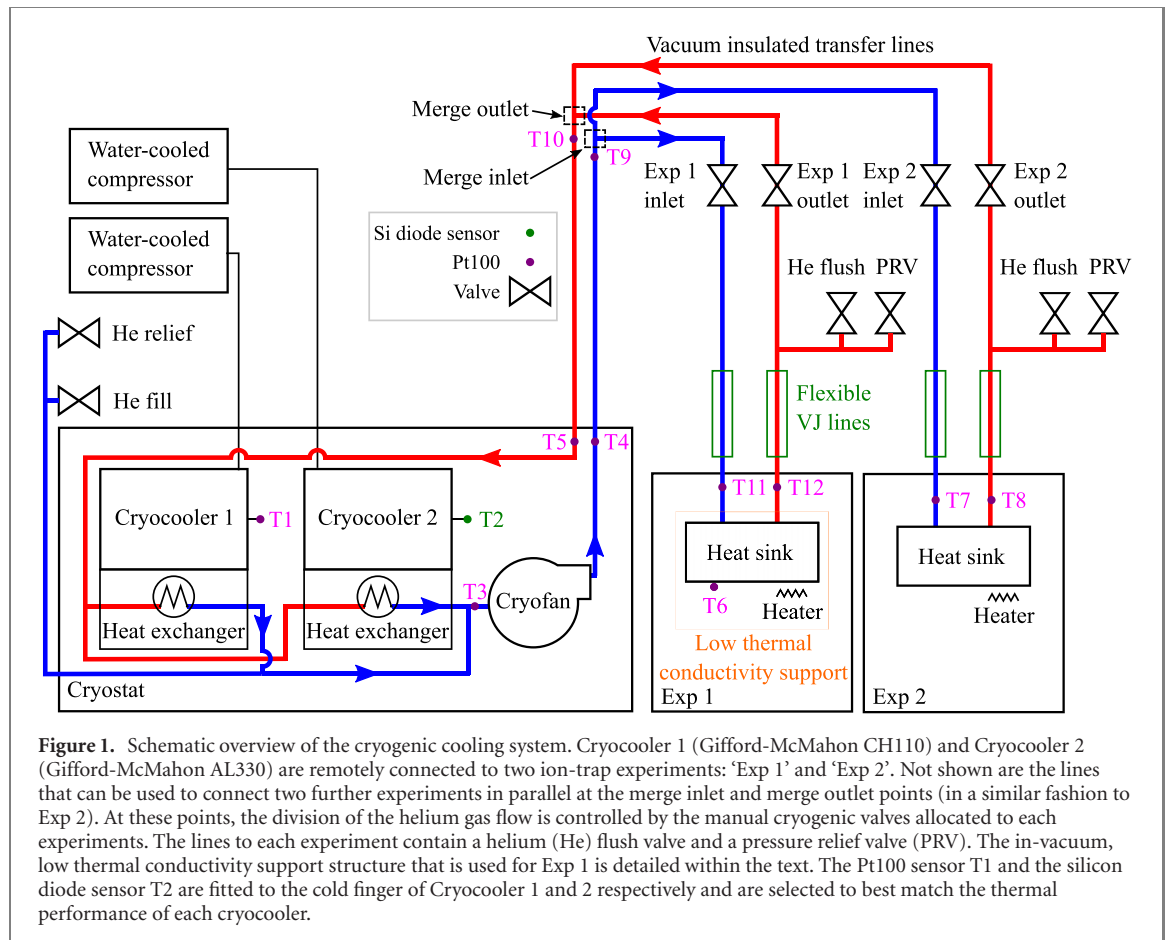
## Abstract

Microfabricated ion-trap devices offer a promising pathway towards scalable quantum computing. Research efforts have begun to focus on the engineering challenges associated with developing large-scale ion-trap arrays and networks. However, increasing the size of the array and integrating on-chip electronics can drastically increase the power dissipation within the ion-trap chips. This leads to an increase in the operating temperature of the ion-trap and limits the device performance. Therefore, effective thermal management is an essential consideration for any large-scale architecture. Presented here is the development of a modular cooling system designed for use with multiple ion-trapping experiments simultaneously. The system includes an extensible cryostat that permits scaling of the cooling power to meet the demands of a large network. Following experimental testing on two independent ion-trap experiments, the cooling system is expected to deliver a net cooling power of 111 W at  $\sim 70$  K to up to four experiments. The cooling system is a step towards meeting the practical challenges of operating large-scale quantum computers with many qubits.

## 1. Introduction

Trapped ions are a leading platform for quantum computers (QCs) [1], quantum simulators [2], high-precision quantum sensors [3, 4] and fundamental physics research [5, 6]. A number of trapped-ion QC architectures have been proposed which focus on developing scalable designs for future fault-tolerant devices with many qubits [7, 8]. Microfabricated ion-traps [9] are a promising architecture for a modular QC [7]. A recently published QC blueprint [7] uses modular surface ion-traps, with integrated on-chip electronics for ion transport, quantum state manipulation and readout. Each addition of these on-chip features, however, increases the power dissipated by components such as radio frequency (RF) conductors, digital-to-analogue converters [10], fluorescence detectors [11], integrated ovens, and magnetic field generating structures [9]. The thermal management of the modular QC is then essential to retain a reasonable operating temperature.

This paper describes the development of a scalable cooling system with novel application to ion-trap devices. Designed as a step towards a scalable cryogenic cooling solution suited to the QC architecture described by Lekitsch *et al* [7], the system uses circulating helium gas to cool multiple ion-trapping experiments independently. Under no active heat load, two ion trap experiments were measured to reach a base temperature of 34 K. However, the system is capable of providing cooling to four ion-trap experiments where one experiment has a high active heat load of 75 W and the remaining have a heat load of 12 W. In this configuration, each of the experiments are expected to operate at  $\sim 70$  K. In addition to managing the thermal loads for an ion-trap experiment, the cooling system may also improve ion-trap performance by suppressing electric field noise [12], leading to a reduction in ion motional heating. For example, with



surface traps with electroplated gold electrodes (that have not had any previous surface treatment such as ion milling [13]) the change in temperature from 300 K to 70 K can reduce the ion heating rate by approximately an order of magnitude [13].

## 2. Design overview

A range of cryogenic cooling solutions have been demonstrated with small-scale ion-trapping experiments. ‘Wet’ systems consist of either an open bath [14–16] or an open continuous flow cryostat [17] that use 4 K liquid helium or 77 K liquid nitrogen as coolant. Cryogenic temperatures are sustained for the duration of the liquid cryogen reserve which is lost to the environment by evaporation. ‘Dry’ cryogenic systems do not require replenishment of cryogen, which is an attractive feature. Instead, cooling is provided by a closed thermodynamic refrigeration cycle. These have found wide application to ion trapping experiments in the form of pulse-tube [18, 19] or Gifford–McMahon (GM) [20, 21] cryocoolers. However, size constraints prevent sufficient numbers of individual, commercially available cryostats from being used together within closely-spaced ion-trap arrays. Therefore, a new cooling architecture that avoids these constraints is proposed. The architecture is based on a closed-loop cryogenic helium gas circulation system; separating the cryocooler from the ion-traps in a way which is in principle extensible to accommodate large numbers of both ion-trap elements and cryocooler cold heads.

A cooling system based on this architecture was constructed to interface between four independent ion-trap experiments. The cooling system consists of three sections: a main cryostat chamber that houses two single-stage Gifford–McMahon cryocooler cold heads and a centrifugal pump; a network of vacuum-jacketed (VJ) helium transfer lines that distribute the cold gas from the cryostat to the ion-trap experiments, and a cryogenic heat sink installed on each experiment. A diagram of the cooling system is shown in figure 1. The cooling system distributes helium gas to multiple experiments configured in parallel. Individual experiments can be connected and disconnected from the cooling circuit independently. Together, the two cryocoolers deliver a total cooling power of 396 W at 80 K [22, 23].

Inside the cryostat chamber, each cold head interfaces with a heat exchanger that is braised to its cold finger. This minimises the thermal resistance between the cold head and heat exchanger carrying the helium

cryogen. The compressors used to operate the cryocoolers are located in a separate room adjacent to the laboratory to minimise vibration at the ion-trap experiments.

Helium gas is circulated using a stirling cryogenics noordenwind centrifugal pump (also referred to as cryogenic fan or ‘cryofan’) with a 31 mm wide impeller which can be throttled between 6000 and 21 000 revolutions per minute (rpm). The flow of helium gas is routed in parallel to the two cold heads via stainless steel tubing and then recombined prior to the inlet of the cryofan. This parallel circuit configuration reduces the overall flow resistance across the cryostat section, while allowing for faster thermalisation of the gas through the heat exchangers. In this configuration the total available cooling power can be scaled by integrating extra cryocoolers in parallel, while the resulting increase in flow resistance can be compensated used a higher capacity cryofan. Within the cryostat vessel, leak-tight connections are made using both vacuum coupling radiation fittings and by direct welding. To assist in damping vibrations caused by the cold heads’ internal displacer, a section of flexible, mesh-reinforced, stainless steel braided hose was installed at the cryofan inlet.

The cryostat vessel and the VJ lines are maintained under vacuum ( $<10^{-4}$  mbar) to prevent conductive heat leaks. The cold heads, cryofan and stainless-steel tubing are lined with 30 layers of multilayer insulation (MLI) to minimise radiative heat leaks. Overall, the transfer lines are expected to contribute to thermal losses by  $0.2 \text{ W m}^{-1}$  across the network, which extends for 30 m.

The cryogen supply and return lines, encased within the VJ lines, are stainless steel with 10 mm inner diameter. At the locations of each ion-trapping experiment, the VJ transfer lines separate into two individual supply and return lines. These are constructed from flexible VJ tubing to further attenuate vibrations from the cryostat and correct for thermal expansion mismatches between sections of different temperatures. This flexible section consists of two coaxial braided corrugated hoses. The inner corrugated hose (Witzenmann, DN10 vibrafex) carries the cryogen and is wrapped in MLI while the outer one (Witzenmann, DN32 vibrafex) acts as a vacuum jacket for thermal insulation. The vacuum of the main VJ line is isolated from the vacuum of the flexible VJ lines, which has to be separately evacuated. Furthermore, the vacuum of the flexible VJ lines is isolated from the ultra-high vacuum (UHV) of the ion-trap experiment. This enables the flexible sections to be disconnected from the vacuum chamber, while maintaining the vacuum insulation within the main VJ transfer line and the UHV within the experiment chamber.

The system is pressurised to 20 bar and the overall helium gas mass flow rate is controlled by adjusting the rotation speed of the cryofan impeller. A schematic of the helium gas transfer network, which connects the cryostat to the ion-trap experiments, is shown in figure 1.

The local flow of helium gas allocated to each ion-trapping experiment is regulated using two manual cryogenic valves (CryoComp, C2041-M21) which are fitted on the feed and return transfer lines. When an experiment is disconnected, the cold pressurised helium gas trapped in the experiment heat sink warms up and expands. A cryogenic safety pressure relief valve (PRV) (Swagelok, SS-43GM4), set to 23 bar, is fitted at the experiment return VJ line to avoid over-pressure in the heat sink during thermalisation to room temperature. An additional valve (‘He flush’ valve in figure 1) connects the inner helium line to atmosphere and allows for each experiment to be evacuated and flushed with helium before being cooled down. Flushing with helium removes any trapped air and water vapour that can freeze on the impeller blades of the cryofan, or inside the heat sink, which may cause damage or choke the helium flow.

### 3. Interfacing with an ion-trap experiment

In each ion-trap experiment, active heat loads arise from various sources, e.g. RF losses within the substrate of the microchips, Ohmic heating within microfabricated wires carrying electrical currents [7, 24], and power dissipation from chip-integrated electronics [10]. Passive heat loads result from both thermal conduction and radiation. Conductive losses occur along solid paths provided by feedthrough connections into the vacuum chamber and by the in-vacuum mounting structure. Radiative heat transfer occurs between the room temperature vacuum apparatus and the cryogenic surfaces that are in direct line of sight.

To minimise the passive thermal load in experiment 1 (Exp 1 in figure 1) a high stability, low thermal conductivity support structure was designed with a large thermal resistance. The design can be seen in figure 2(a). The mounting structure supports two ion-trap chips which are not shown in the figure. This experiment was designed with the objective of demonstrating shuttling-based connectivity between trapped ion QC modules as proposed by Lekitsch *et al* [7]. One ion-trap (ion-trap 1 in figure 2(a)) is mounted to the heat sink and a second ion-trap (ion-trap 2 in figure 2(a)) is mounted on the adjacent structure with cooling provided by a flexible copper braid that thermally anchors it to the first.

The heat sink that interfaces an ion-trap with the cooling system can be seen in figure 2(b). It consists of a compact, stainless steel/OFHC copper enclosure within which cold helium gas is circulated. The heat sink

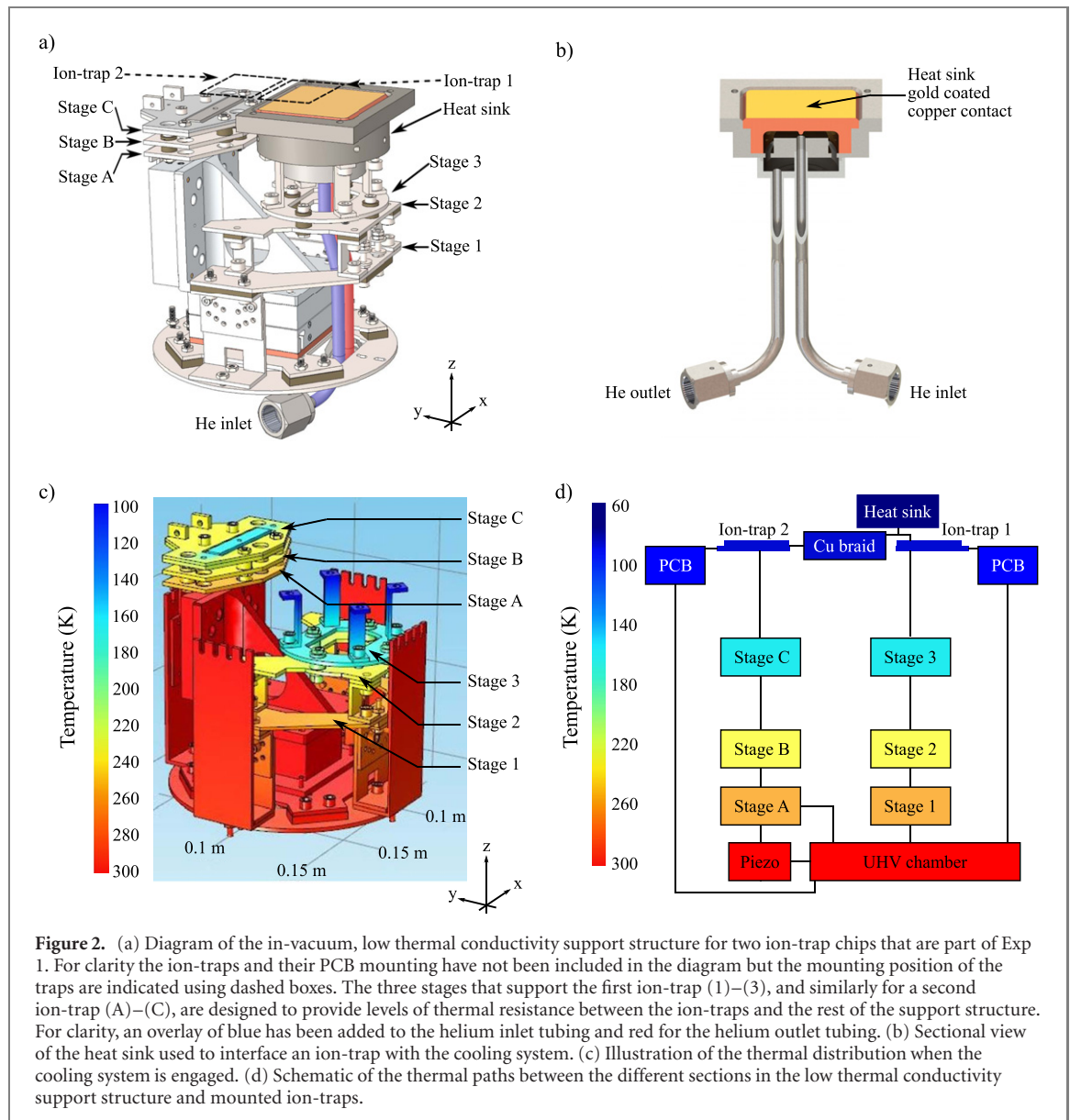


**Figure 2.** (a) Diagram of the in-vacuum, low thermal conductivity support structure for two ion-trap chips that are part of Exp 1. For clarity the ion-traps and their PCB mounting have not been included in the diagram but the mounting position of the traps are indicated using dashed boxes. The three stages that support the first ion-trap (1)–(3), and similarly for a second ion-trap (A)–(C), are designed to provide levels of thermal resistance between the ion-traps and the rest of the support structure. For clarity, an overlay of blue has been added to the helium inlet tubing and red for the helium outlet tubing. (b) Sectional view of the heat sink used to interface an ion-trap with the cooling system. (c) Illustration of the thermal distribution when the cooling system is engaged. (d) Schematic of the thermal paths between the different sections in the low thermal conductivity support structure and mounted ion-traps.

uses a jet-impingement design where the pressurised helium jet is directed onto a copper plate, which is used as the heat transfer interface (see figure 2(b)). This approach generates only a small pressure drop over a large range of flow rates. Alternative heat sink designs, such as ones using pins, fins or microchannels may deliver improved heat transfer performance but carry the risk of a larger pressure drop penalty [25] while also being more complex to manufacture [26]. These designs remain under consideration for future upgrades of the system. In order to interface with the ion-trap, the heat sink copper plate is coated with  $3\ \mu\text{m}$  of gold and an additional copper support is added onto which the trap is then die-bonded. The gold-plated copper to copper structure ensures good thermal anchoring with an expected thermal contact conductance of  $1.1\ \text{W K}^{-1}\ \text{cm}^{-2}$  [27, 28]. A  $50\ \Omega$  cryogenic heater (Lakeshore, HTR-50), capable of continuous operation under 1 A, is used to stabilise the heat sink temperature through a control loop and for warm-up. Electrical connections to the heater are made using 0.4 mm diameter cables which carry a conductive heat load from the environment that is estimated to be 0.5 W.

The support structure around the heat sink reduces the conductive and radiative heat transfer from the surrounding vacuum chamber, effectively minimising the passive heat load on the heat sink. The structure is subdivided into three stages operating at different temperatures. Each stage of the assembly is built with grade 5 titanium alloy (Ti6Al4V) owing to its low thermal conductivity ranging from 1 to  $3\ \text{W m}^{-1}\ \text{K}^{-1}$ , and low coefficient of thermal expansion in the 20–100 K temperature range [29]. These are respectively one third and one half of that of stainless steel over the same temperature range [29]. An approach to further increase the thermal insulation of the support structure is to prevent metal-to-metal contacts between the cryogenic support stages. For this purpose, UHV compatible PEEK spacers were used between

stages to minimise conductive losses as they increase the overall thermal path while having a low thermal conductivity at cryogenic temperatures [30]. A three-dimensional, finite element method simulation of the conductive heat transfer through the support structure geometry was carried out using COMSOL and accounts for the thermal conductivity of the materials used. A visualisation of the temperature distribution on the support structure is provided in figure 2(c). Overall, the structure exhibits a total thermal resistance of 146 K/W between ion-traps at 70 K and the room-temperature vacuum chamber leading to a conductive thermal leak of 1.7 W. A schematic of the thermal paths between the vacuum chamber and the ion-traps can be seen in figure 2(d). Furthermore, the titanium alloy parts are also electromechanically polished. This minimises their emissivity, thereby mitigating radiative heat transfer from the outer room-temperature vacuum chamber walls. By modelling the assembly as having grey-diffuse surfaces, the heat load from thermal radiation is estimated to be 2.5 W.

Thermometry is provided using class A platinum resistance temperature sensors (Pt100s) (RS pro, 293-8468). Each sensor is thermally anchored using a spring loaded copper clamp. The electrical connections to each sensor are made in the four-wire configuration using long, phosphor-bronze cables which have reduced thermal conductivity compared to copper. The conductive heat load due to the electrical wiring to the sensors is estimated to be 15 mW per sensor.

## 4. Testing and characterisation

The performance of the cooling system was evaluated in a set of cryogenic tests that were carried out first with a single ion-trap experiment, and then with two experiments connected in parallel to the cooling system. The results in the following sections demonstrate the minimum operating temperature of the system, the time to reach a steady state, and the frequency and amplitude of vibrations at the ion-trap locations.

### 4.1. Cooling of a single ion-trap experiment under no active heat load

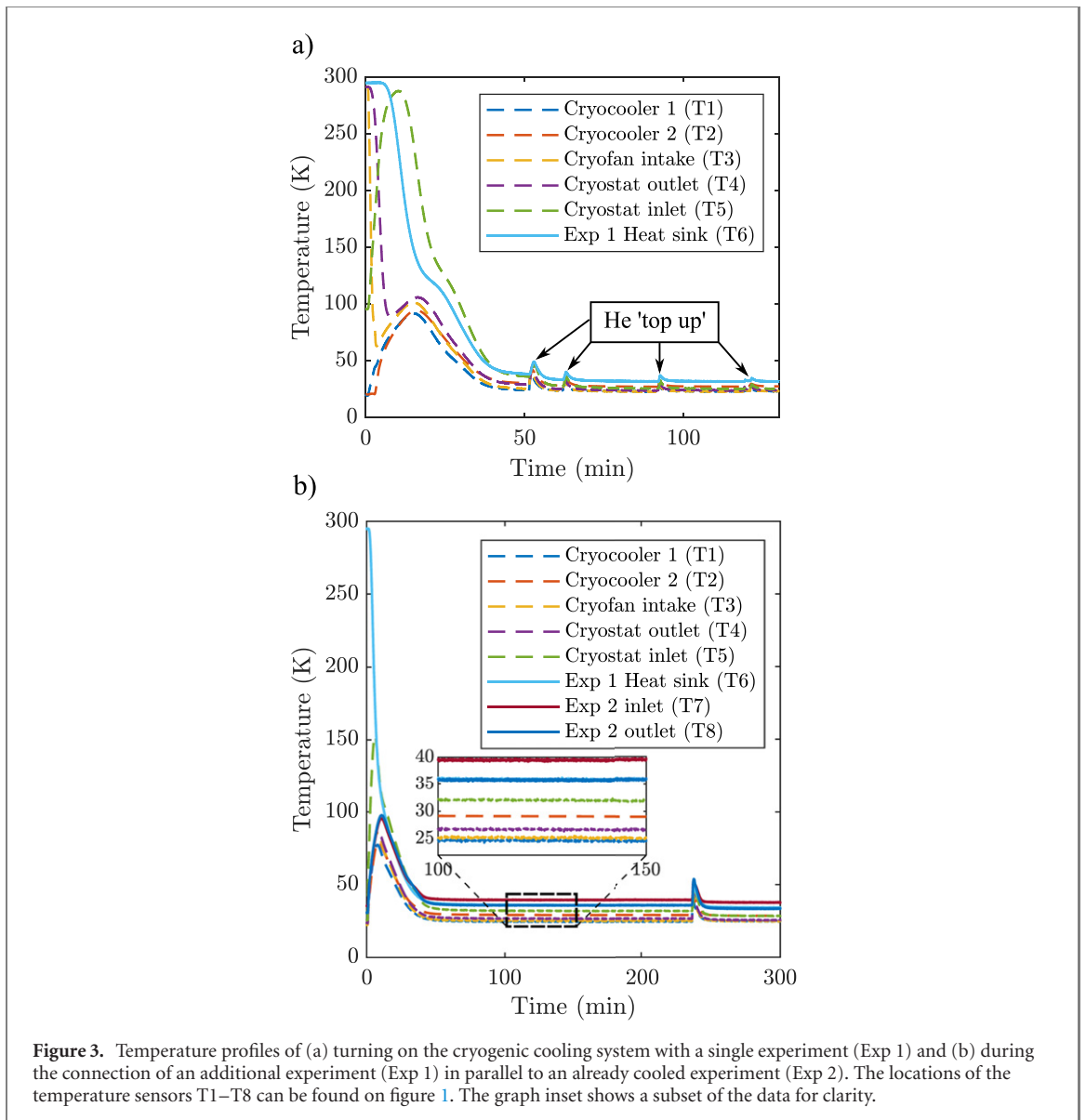
Here the cooling system performance is investigated when connected to a single experiment (Exp 1 in figure 1). Initially, there are no experiments connected and the cryofan is turned off. Therefore, since there are minimal heat loads present, both cryocoolers were allowed to reach their base operating temperature of  $\sim 20$  K. The cooling system was then connected to a single ion-trap experiment (Exp 1 in figure 1). The system was filled with helium gas and pressurised to 20 bar. To circulate helium to the experiment, the valves controlling the helium flow to the heat sink at the ion-trap experiment were fully opened. The cryofan was then switched on and set at its maximum rotation speed of 21 000 rpm.

Figure 3(a) shows the evolution of the temperature of the cooling circuit when an experiment at room-temperature is connected. For this test, a silicon diode sensor and Pt100 temperature sensors were installed into the system as indicated by figure 1. Helium gas circulates from the cold head heat exchangers to the cryofan and exits the cryostat vessel at the maximum flow rate. This resulted in cryogenic temperatures ( $\leq 100$  K) measured at the cryofan intake and the cryostat outlet locations within 7 min of activating the cryofan.

As the cold helium gas circulates through the transfer lines to the heat sink at the ion-trap experiment, it displaces room temperature gas within the lines. As a consequence, the cryostat inlet sensor measures a transient rise in temperature. This effect was also measured to a lesser extent by the other sensors throughout the circuit. After 15 min, the rising temperature reaches a maximum and begins to decrease. Within 30 min of activating the cryofan, all sensor readings were below 40 K.

Since the helium pressure decreases with temperature, additional ‘topping-up’ of gas was required to maintain a 20 bar operating pressure. These top-ups were performed four times over the course of  $\sim 90$  min, until the temperature and pressure stabilised. In order to assess the rate of thermal contraction for a particular application it may be relevant to note the maximum cooling rate. Here the maximum cooling rate at the experiment heat sink was measured to be  $23 \text{ K min}^{-1}$ . Full control of the cooling rate is also possible by manually adjusting the inlet and return helium valves. The highest cooling rate of all sensor locations was  $150 \text{ K min}^{-1}$ , measured at the cryofan intake. A steady-state base temperature of 31.6(6) K was reached at the experiment heat sink after 3 hr of operation under no active heat load.

During the cool down of the assembly, thermo-mechanical effects lead to a relative displacement of the three stages that support ion-trap 1 and ion-trap 2 (see figure 2(a)). Displacements must be taken into account during room-temperature installation of the system to prevent the two ion-trap chips from colliding at cryogenic temperatures. The low thermal conductivity support structure was designed to ensure that the ion-traps remain apart during bake-out and approach each other during controlled cool down. FEM simulations were used to anticipate the effect of thermal contraction and the displacement occurs primarily along the  $z$  and  $y$  axes. Relative displacements were expected to be  $250 \mu\text{m}$  along  $z$ , such that



**Figure 3.** Temperature profiles of (a) turning on the cryogenic cooling system with a single experiment (Exp 1) and (b) during the connection of an additional experiment (Exp 1) in parallel to an already cooled experiment (Exp 2). The locations of the temperature sensors T1–T8 can be found on figure 1. The graph inset shows a subset of the data for clarity.

ion-trap 1 would translate below ion-trap 2. Displacements of  $60 \mu\text{m}$  were also expected along  $y$ , such that the structure supporting both chips move towards one another. Baking the system at  $140^\circ\text{C}$ , was also found to result in a relative displacement of the two trap support sub-assemblies. These were measured to be of  $335(5) \mu\text{m}$  along  $x$  and  $26(5) \mu\text{m}$  along  $y$ . These offsets are attributed to the relaxation of stress during thermal cycling. During cool down, we observe displacements matching our numerical simulation with minor additional misalignment (on the order of 10 s of microns).

To scale beyond the two ion-traps support structure presented in this work, a single rigid support structure (as used in [7]) would be beneficial to minimise displacements during large temperature cycles. A more rigid structure would prevent any mechanical conflicts between traps that are aligned together while in-vacuum piezo actuators can be used to correct for minor misalignments following cool down.

#### 4.2. Cooling of two ion-trap experiments under no active heat load

This section investigates how connecting and disconnecting an experiment to the cooling system influences its overall performance. For this purpose, Exp 1 was connected into the cooling system circuit following cooling of Exp 2 to  $31.6(6) \text{K}$ . Similar platinum temperature sensors are used in Exp 2 as in Exp 1. The temperature evolution of Exp 1 is shown in figure 3(b).

The cryogenic helium gas valves were opened at Exp 1 to allow cold helium gas at  $32 \text{K}$  to circulate. For Exp 2, in place of a heat sink, a length of  $1/4''$  copper pipe was installed with two Pt100 sensors at the inlet and outlet of the copper fitting. As the valves to Exp 1 were opened a transient temperature rise was observed. At Exp 2 the temperature rises for 11 min until a maximum temperature of  $97.7(5) \text{K}$  is reached, before decreasing to  $36.3(6) \text{K}$  60 min after the start of the test sequence. At Exp 1, the heat sink reaches

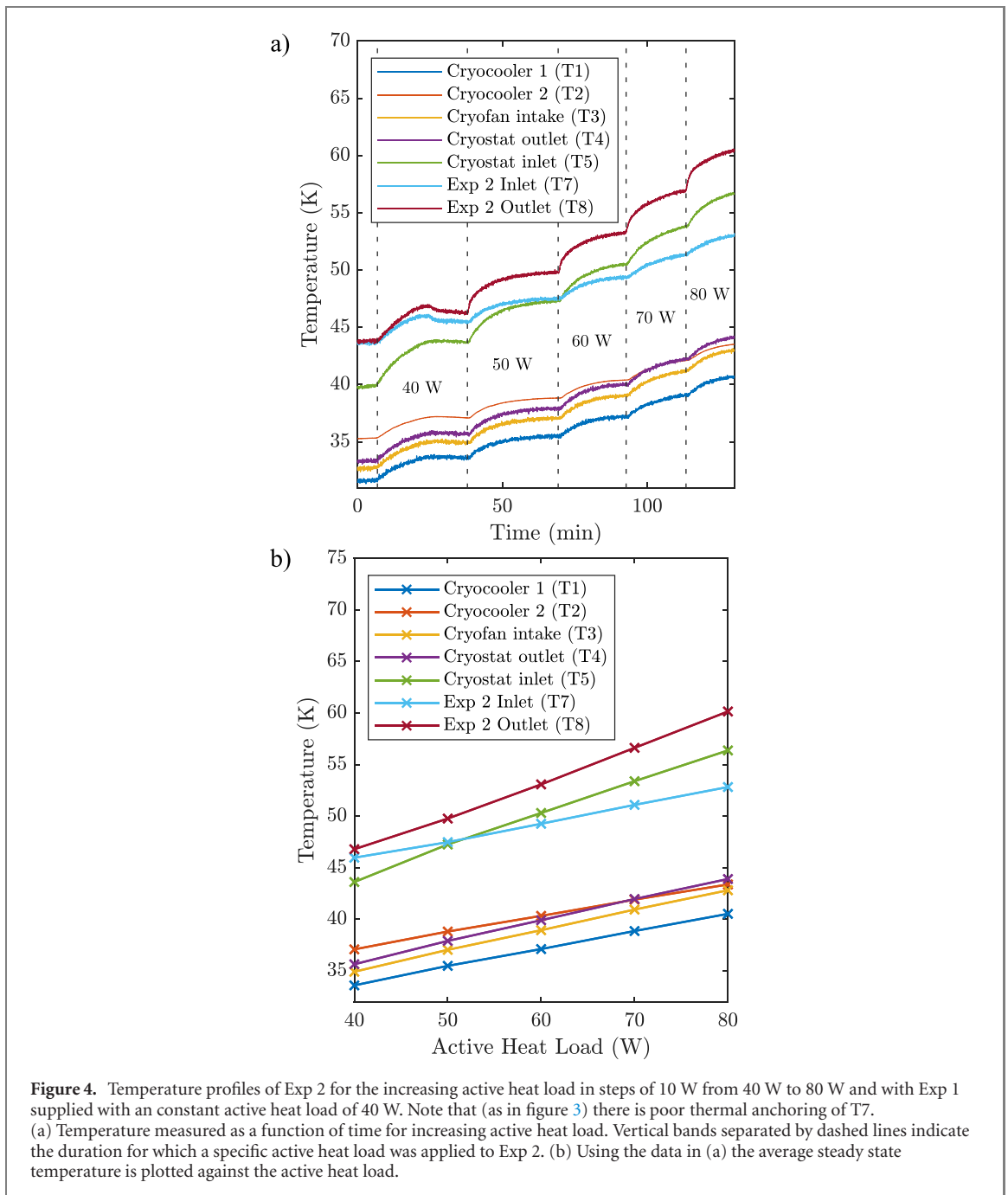


**Figure 4.** Temperature profiles of Exp 2 for the increasing active heat load in steps of 10 W from 40 W to 80 W and with Exp 1 supplied with an constant active heat load of 40 W. Note that (as in figure 3) there is poor thermal anchoring of T7. (a) Temperature measured as a function of time for increasing active heat load. Vertical bands separated by dashed lines indicate the duration for which a specific active heat load was applied to Exp 2. (b) Using the data in (a) the average steady state temperature is plotted against the active heat load.

36.7(6) K after 60 min. A single helium gas top-up to 20 bar was performed. This led to a temporary spike in temperature, before settling to a steady-state temperature of 34.3(6) K at Exp 1 and 33.5(6) K at Exp 2.

Under no active load, the steady-state temperature at the outlet is expected to be marginally higher than that of the inlet owing to the passive thermal leaks to the experiment heat sink. However, the inlet temperature (39.5 K) is measured to be higher than that of the outlet (36 K). This effect is attributed to unequal thermal anchoring of the sensors to the helium lines and the passive heat load from connecting wires conducted from the environment.

#### 4.3. Active heat load tests

This section investigates the relative contribution of active and passive heat loads in the cooling circuit. At thermal steady-state, the total cooling power of the cryogenic system is equal to the sum of the active and passive heat loads.

The cooling power was measured directly by applying an electric current to a heater installed within each ion-trap experiment (see figure 1). This is a variable active heat load that is directly delivered to the ion-trap. This heat load was increased in steps of 10 W to a maximum of 80 W. The temperature of the heat sink outlet was monitored until steady-state was reached for a given active heat load. This procedure was

reproduced separately for Exp 1 and Exp 2 as well as when an active heat load was applied to both experiments with the system operated under 23 bar. Figure 4 shows an example of the active heat load at Exp 2 being incrementally adjusted from 40 W to 80 W while the active heat load supplied to Exp 1 was held constant at 40 W. With 80 W of applied heat load, the temperature at Exp 2 remains significantly under 100 K.

The cold head capacity curves provided by the manufacturer [22, 23], establish the dependency of the cooling power with temperature. Therefore, the total heat load can be calculated from the temperature of the cold heads. By subtracting the known active heat loads applied to the experiment heat sink, the passive heat loads were calculated. The total passive heat load calculated on the cooling system was 86(3) W when connected to the first experiment and 78(4) W when only connected to the second. When the two experiments were connected in parallel the total passive heat load was 108(3) W.

By comparing the results for experiments connected first individually and then in parallel, the contributions to the passive heat load from each section of the cooling circuit can be distinguished. The cryostat vessel is subject to a passive heat load of 56(3) W, while the first and second experiments (including their circuit loops) contribute 30(4) W and 22(3) W, respectively.

#### 4.4. Helium gas flow rate

Understanding the fluid flow dynamics of the single- and two-ion trap experiment is necessary to predict the system performance as it is extended to provide cooling to additional experiments. The total volume flow rate  $\dot{V}$  is inversely proportional to the temperature difference  $\Delta T$  (K) between the cryostat inlet (T5) and cryofan intake (T3), as described by [31]

$$\dot{V} = \frac{\dot{Q}}{c_p \rho_{\text{He}} \Delta T}, \quad (1)$$

where  $\dot{Q}$  is the total cooling power (W),  $c_p$  is the specific heat capacity of helium at constant pressure ( $5.517 \text{ J g}^{-1} \text{ K}^{-1}$ ), and  $\rho_{\text{He}}$  is the helium density ( $\text{kg m}^{-3}$ ). When the cooling system is connected to two experiments in parallel, the maximum volume flow rate,  $\dot{V}$ , is  $0.40 \text{ m}^3 \text{ hr}^{-1}$  for a cryofan rotation speed of 21 000 rpm. From the cryofan specifications, the total pressure drop was estimated across the circuit to be 9.8 kPa [32].

However, calculation of the local flow rate at each experiment using equation (1) was not possible due to measurement offsets. These offsets were attributed to poor thermal anchoring of the Pt100 sensors, which was due to thermal contraction mismatches during cool down. Instead, a calculation of the volume flow rate at a single experiment  $\dot{V}_{\text{exp}}$  is made via a rearrangement of equation (1) using two consecutive measurements such that

$$\dot{V}_{\text{exp}} = \frac{\Delta \dot{Q}}{c_p \rho_{\text{exp}} (\Delta T_{\text{out}} - \Delta T_{\text{in}})}, \quad (2)$$

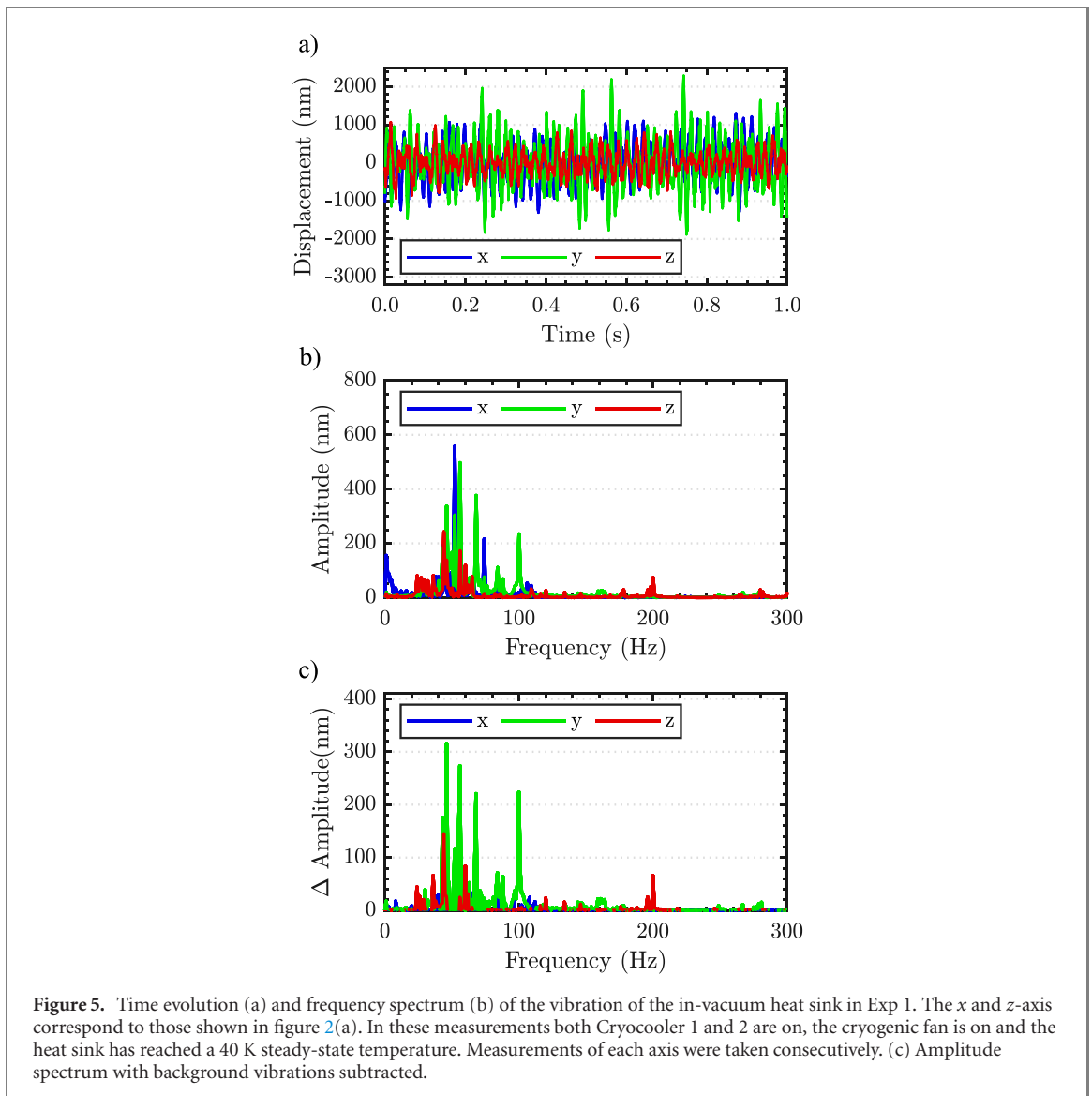
where  $\Delta \dot{Q}$  (W) is the power difference between two heat loads applied consecutively at the ion-trap,  $\rho_{\text{exp}}$  is the helium density at the experiment location, and  $\Delta T_{\text{in}}$  (K) and  $\Delta T_{\text{out}}$  (K), are the steady-state temperature differences measured at the inlet and outlet locations respectively. Using equation (2), a helium volume flow rate of  $0.24 \text{ m}^3 \text{ hr}^{-1}$  and  $0.16 \text{ m}^3 \text{ hr}^{-1}$  is calculated for the first and second experiment respectively. The larger flow rate at Exp 1 is essential since it contains a larger number of heat dissipating components than Exp 2 and therefore requires more cooling power. When combined, these volume flow rates are consistent with the total volume flow rate  $\dot{V}$  calculated at the cryostat.

No significant change in the total flow rate was observed during the process of connecting an experiment into the cooling circuit.

#### 4.5. Vibrations

While the combination of two GM cryocoolers delivers substantial cooling power at 70 K, the operation of the cryocooler cold heads generates significant vibration, which requires damping. Measurements with piezo-electric accelerometers (DYTRAN, 3143M1) of the cryostat vessel, which houses the cold heads, show maximum displacement occurs at frequencies of 2 Hz and 50 Hz, with large amplitudes of  $50 \mu\text{m}$  and  $3 \mu\text{m}$  respectively.

To reduce the amplitude of vibrations transmitted from the cryostat vessel to the ion-trap experiments, a number of vibration damping measures were taken onto the helium transfer lines. The vacuum jacket surrounding the transfer lines is mechanically decoupled from the cryostat via edge-welded bellows. The



lines have flexible sections installed at locations close to the helium feedthroughs on each vacuum chamber. Additionally, each vacuum chamber is rigidly anchored to a massive 545 kg optical table (Thorlabs, T1225CN), thereby downshifting the natural resonant frequency of the mechanical system past the flexible VJ lines.

Vibration measurements were made at the ion-trap experiment closest to the cryostat, using a heterodyne Michelson interferometer set-up (in a similar fashion to that presented in reference [17]). Three mirrors were attached to the ion-trap support structure inside the vacuum chamber to reflect 650 nm laser light delivered along three perpendicular axes. Reference mirrors were anchored directly onto the outside of the vacuum chamber. This method permits measurements of vibrations with amplitudes of a few nm and in the frequency range 0–50 kHz.

When the heat sink is operating at 40 K, the measured vibration can be seen in figure 5(a) which shows the largest vibrations are in the  $y$ -direction with a maximum displacement of  $2.3 \mu\text{m}$  relative to the vacuum chamber. Figure 5(b) shows the frequency spectrum of the vibration as calculated from figure 5(a). However, the measurements in figure 5(b) are the total vibrations experienced by the experiment. To isolate the effect of the cooling system, measurements at 295 K were also taken. Figure 5(c) shows the difference in the amplitudes of vibration between when the cooling system was turned on (figure 5(b)) and turned off. The most prominent contributions from the cooling system are in the  $y$ -direction at 46 Hz, 56 Hz, 68 Hz and 100 Hz with amplitudes of 315 nm, 274 nm, 220 nm and 224 nm respectively.

The measured vibration amplitudes are acceptable for intended ion trapping experiments as coherent qubit manipulation will be driven using microwave and RF radiation. In this scheme, laser fields are solely used for photo-ionisation, Doppler cooling, state initialisation and detection. For these purposes, Exp 1 uses a 369.5 nm laser with a Gaussian beam profile and a  $50 \mu\text{m}$  waist. Given a  $2.3 \mu\text{m}$  displacement of the ion

**Table 1.** Summary of temperature projections for Exp 1 and 2 when configured for four ion-trap experiments connected in parallel. The additional two ion-trap experiments are expected to perform similarly as Exp 2. All four experiments are expected to operate below 70 K as given by the average temperature between inlet and outlet within each set-up. An explanation of the positions labelled in the table can be found in figure 1.

Position	Temperature (K)
Cryocooler 1 (T1)	51.0
Cryocooler 2 (T2)	55.1
Cryofan intake (T3)	53.0
Cryostat outlet (T4)	55.0
Cryostat inlet (T5)	79.5
Merge inlet (T9)	58.5
Merge outlet (T10)	82.5
Exp 1 inlet (T11)	62.0
Exp 1 outlet (T12)	79.0
Exp 2 inlet (T7)	65.0
Exp 2 outlet (T8)	70.5

relative to the centre of the beam, a 2% intensity fluctuation is expected. However, this fluctuation is negligible as the dominant source of intensity noise ( $\sim 4\%$ ) arises from the laser light source.

For laser-based quantum logic experiments, additional vibration damping and isolating measures may be taken to meet stringent laser-phase stability conditions with respect to the trapped ion. Limiting further ion-trap displacements to less than 100 nm may be realised by routing the transfer lines through large sand boxes or by attaching tuned damping springs to absorb vibrations. Vibrations may also be eliminated near the source by mechanically decoupling the cryostat from the cold head using flexible copper braids [18, 19] or a helium buffer gas [16, 21].

Implementing vibration isolation techniques would also be beneficial when scaling to large precisely aligned ion-trap arrays. Improved isolation would reduce the difficulty in achieving and maintaining laser beam alignment. However, a similarly negligible contribution to laser intensity fluctuations can be realised using integrated on-chip optical elements which ensure inherent resilience to vibrations [33]. Mechanical vibrations can also adversely affect the ability to maintain precise alignment between ion-traps. An architecture constructed from identical ion-traps mounted to the same rigid support structure are expected to share the same resonant frequency and therefore mode of vibration. Considering the worst-case scenario of asynchronous oscillation between ion-traps, the relative displacement may be as high as  $2 \times 2.3 \mu\text{m} = 4.6 \mu\text{m}$ . However, numerical simulations presented in [7] suggest that chip misalignment up to  $10 \mu\text{m}$  remain suitable for reliable qubit transport between ion-traps. Current level of vibrations are therefore acceptable provided chips are initially aligned within  $5 \mu\text{m}$  of one another.

## 5. Scaling from two to four ion-trap experiments

In this section, we present a model of the cooling system performance when operating with four experiments connected in parallel. This model was derived from results presented in sections 4.3 and 4.4 where we discussed the active heat load tests and characterised the helium flow rate across two ion-trap experiments. This model assumes a total volume flow rate,  $\dot{V}$ , of  $0.40 \text{ m}^3 \text{ hr}^{-1}$ . The passive heat load is assumed to be 60 W at the cryostat, which is an overestimate of the 56(3) passive heat load presented in section 4.3. For each of the four parallel circuit loops, the local passive heat loads are then assumed to be of 30 W. These are also conservative estimates considering our previous measurements of passive heat loads within the circuit loop to Exp 1 and Exp 2. For the four ion-trap experiments, an active heat load of 75 W is assumed for the first and 12 W each is assumed for the others. These ‘power budgets’ were chosen based on the number of active components within each ion-trap experiment. The total heat load is therefore 291 W, of which 111 W are active and 180 W are passive. Cryocooler 1 and 2 are expected to operate at 51 K and 55 K, respectively [22, 23].

At this temperature and under a pressure of 20 bar, the helium gas density at the cryofan is calculated to be  $18.16 \text{ kg m}^{-3}$ . The equivalent mass flow rate at the cryostat is therefore projected to be  $2.01 \text{ g s}^{-1}$ . The valves at each experiment are set to divide the flow rate such that  $0.81 \text{ g s}^{-1}$  of helium is delivered to the 75 W experiment while  $0.40 \text{ g s}^{-1}$  is delivered to each of the three 12 W experiments. Average heat sink temperatures of 65.5 K and 68 K are expected at Exp 1 and Exp 2 respectively. The additional two experimental ion-trapping set-ups are expected to perform similarly as Exp 2, such that all four ion-trap

experiments are projected to operate below 70 K. Table 1 provides a summary of the temperature projections of the model. At this temperature we anticipate a reduction of the ion heating rate across all four experiments by about an order of magnitude compared to room-temperature operation [13].

## 6. Conclusion

Thermal management is a critical concern within a scalable architecture for ion-trap quantum computing. Presented here is the development of a cryogenic cooling system with high cooling power and a scalable design, applicable to large-scale arrays of ion-traps. This paper demonstrates a laboratory configuration capable of providing 111 W of net cooling power at 70 K to up to four independent ion-trap experiments. By using a remote cryostat that is thermally coupled to a helium gas circulation system, the physical size constraints of existing cryostat systems are no longer an obstacle at the ion-trap location. Therefore, cooling power can be delivered within the constrained footprint area of the ion-trap chips to permit many chips to be closely spaced side by side across a surface. The cooling system therefore satisfies one of the key engineering requirements of the scalable architecture proposed by Lekitsch *et al* [7], and it is a step towards the construction of practical devices for ion-trap quantum information processing. In addition, the system presented here also has applications in other high-power processes that require a scalable distributed cooling network in a similar temperature range. Some examples include high-temperature superconductor technologies [34], cooling of high-power laser amplifiers [35] and even in propellant tanks for space exploration [36].

## Acknowledgements

The authors thank Christophe Valahu for providing valuable technical assistance, Bjoern Lekitsch for helpful guidance during planning of the cooling system, Tomas Navickas for his advice on heat sink construction, and Quentin Bodart for the helpful discussions and comments on this manuscript. This work was supported by the UK Engineering and Physical Sciences Research Council via the EPSRC Hub in Quantum Computing and Simulation (EP/T001062/1), the UK Quantum Technology hub for Networked Quantum Information Technologies (No. EP/M013243/1), the European Commission's Horizon-2020 Flagship on Quantum Technologies Project No. 820314 (MicroQC), the US Army Research Office under Contract No. W911NF-14-2-0106, the Office of Naval Research under Agreement No. N62909-19-1-2116, the Luxembourg National Research Fund (FNR) (Project Code 11615035), the University of Sussex, and through a studentship in the Quantum Systems Engineering Skills, the Engineering and Physical Sciences Research Council (EP/S021582/1) via the Centre for Doctoral Training at the University College London & Training Hub at Imperial College London funded by the EPSRC (EP/P510257/1).

## Data availability statement

The data that support the findings of this study are available upon reasonable request from the authors.

## ORCID iDs

F R Lebrun-Gallagher  <https://orcid.org/0000-0003-4944-8132>

S J Hile  <https://orcid.org/0000-0002-3179-0602>

A Owens  <https://orcid.org/0000-0001-8374-4627>

F Bonus  <https://orcid.org/0000-0002-8956-8887>

W K Hensinger  <https://orcid.org/0000-0001-8329-438X>

## References

- [1] Bruzewicz C D, Chiaverini J, McConnell R and Sage J M 2019 Trapped-ion quantum computing: progress and challenges *Appl. Phys. Rev.* **6** 021314
- [2] Blatt R and Roos C F 2012 Quantum simulations with trapped ions *Nat. Phys.* **8** 277–84
- [3] Biercuk M J, Uys H, Britton J W, VanDevender A P and Bollinger J J 2010 Ultrasensitive detection of force and displacement using trapped ions *Nat. Nanotechnol.* **5** 646–50
- [4] Goldstein G, Cappellaro P, Maze J R, Hodges J S, Jiang L, Sørensen A S and Lukin M D 2011 Environment-assisted precision measurement *Phys. Rev. Lett.* **106** 140502
- [5] Massar S, Spindel P, Varón A F and Wunderlich C 2015 Investigating the emergence of time in stationary states with trapped ions *Phys. Rev. A* **92** 030102

- [6] Horvath G Z K, Thompson R C and Knight P L 1997 Fundamental physics with trapped ions *Contemp. Phys.* **38** 25–48
- [7] Lekitsch B, Weidt S, Fowler A G, Mølmer K, Devitt S J, Wunderlich C and Hensinger W K 2017 Blueprint for a microwave trapped ion quantum computer *Sci. Adv.* **3** e1601540
- [8] Monroe C, Raussendorf R, Ruthven A, Brown K R, Maunz P, Duan L-M and Kim J 2014 Large-scale modular quantum-computer architecture with atomic memory and photonic interconnects *Phys. Rev. A* **89** 022317
- [9] Romaszko Z D, Hong S, Siegle M, Puddy R K, Lebrun-Gallagher F R, Weidt S and Hensinger W K 2020 Engineering of microfabricated ion traps and integration of advanced on-chip features *Nat. Rev. Phys.* **2** 285–99
- [10] Stuart J, Panock R, Bruzewicz C D, Sedlacek J A, McConnell R, Chuang I L, Sage J M and Chiaverini J 2019 Chip-integrated voltage sources for control of trapped ions *Phys. Rev. Appl.* **11** 024010
- [11] Slichter D H, Verma V B, Leibfried D, Mirin R P, Nam S W and Wineland D J 2017 UV-sensitive superconducting nanowire single photon detectors for integration in an ion trap *Opt. Express* **25** 8705
- [12] Labaziewicz J, Ge Y, Leibbrandt D R, Wang S X, Shewmon R and Chuang I L 2008 Temperature dependence of electric field noise above gold surfaces *Phys. Rev. Lett.* **101** 180602
- [13] Brown K R, Chiaverini J, Sage J M and Häffner H 2021 Materials challenges for trapped-ion quantum computers *Nat. Rev. Mater.* **6** 892–905
- [14] Poitzsch M E, Bergquist J C, Itano W M and Wineland D J 1996 Cryogenic linear ion trap for accurate spectroscopy *Rev. Sci. Instrum.* **67** 129–34
- [15] Deslauriers L, Olmschenk S, Stick D, Hensinger W K, Sterk J and Monroe C 2006 Scaling and suppression of anomalous heating in ion traps *Phys. Rev. Lett.* **97** 103007
- [16] Antohi P B, Schuster D, Akselrod G M, Labaziewicz J, Ge Y, Lin Z, Bakr W S and Chuang I L 2009 Cryogenic ion trapping systems with surface-electrode traps *Rev. Sci. Instrum.* **80** 013103
- [17] Brandl M F *et al* 2016 Cryogenic setup for trapped ion quantum computing *Rev. Sci. Instrum.* **87** 113103
- [18] Schwarz M *et al* 2012 Cryogenic linear Paul trap for cold highly charged ion experiments *Rev. Sci. Instrum.* **83** 083115
- [19] Vittorini G, Wright K, Brown K R, Harter A W and Doret S C 2013 Modular cryostat for ion trapping with surface-electrode ion traps *Rev. Sci. Instrum.* **84** 043112
- [20] Sage J M, Kerman A J and Chiaverini J 2012 Loading of a surface-electrode ion trap from a remote, precooled source *Phys. Rev. A* **86** 013417
- [21] Pagano G *et al* 2018 Cryogenic trapped-ion system for large scale quantum simulation *Quantum Sci. Technol.* **4** 014004
- [22] Cryomech Inc 2019 Al330 capacity curve at 50 Hz ([https://cryomech.com/wp-content/uploads/2018/11/AL330W\\_cc.pdf](https://cryomech.com/wp-content/uploads/2018/11/AL330W_cc.pdf))
- [23] SHI Cryogenics Group 2020 Shi cryogenics group, CH-110 capacity curve at 50 Hz ([https://shicryogenics.com/wp-content/uploads/2020/09/CH-110\\_Capacity\\_Map.pdf](https://shicryogenics.com/wp-content/uploads/2020/09/CH-110_Capacity_Map.pdf))
- [24] Ospelkaus C, Warring U, Colombe Y, Brown K R, Amini J M, Leibfried D and Wineland D J 2011 Microwave quantum logic gates for trapped ions *Nature* **476** 181–4
- [25] Kandlikar S G 2005 High flux heat removal with microchannels—a roadmap of challenges and opportunities *Heat Transfer Eng.* **26** 5–14
- [26] Dixit T and Ghosh I 2015 Review of micro- and mini-channel heat sinks and heat exchangers for single phase fluids *Renew. Sustain. Energy Rev.* **41** 1298–311
- [27] Salerno L J and Kittel P 1997 Nasa technical memorandum 110429: thermal contact conductance *Technical Report 19970026086* NASA Ames Research Center, Moffett Field California, US
- [28] Mykhaylyk V B, Burt M, Ursachi C and Wagner A 2012 Thermal contact conductance of demountable in vacuum copper–copper joint between 14 and 100 K *Rev. Sci. Instrum.* **83** 034902
- [29] Marquardt E D, Le J P and Radebaugh R 2002 Cryogenic material properties database *Cryocoolers* vol 11 (Berlin: Springer) pp 681–7
- [30] Ventura G, Bianchini G, Gottardi E, Peroni I and Peruzzi A 2001 Thermal conductivity of peek at low temperatures *Proc. 8th Int. Symp. Temperature and Thermal Measurements in Industry and Science* vol 2 pp 1151–5
- [31] Incropera F P, DeWitt D P, Bergman T L and Lavine A S 2006 *Fundamentals of Heat and Mass Transfer* (New York: Wiley)
- [32] Stirling Cryogenics B.V. 2020 The cryofan range ([https://stirlingcryogenics.eu/files/\\_documents/1/CryofansDatashet.pdf](https://stirlingcryogenics.eu/files/_documents/1/CryofansDatashet.pdf))
- [33] Niffenegger R J *et al* 2020 Integrated multi-wavelength control of an ion qubit *Nature* **586** 538–42
- [34] Pamidi S, Kim C H and Graber L 2015 High-temperature superconducting (HTS) power cables cooled by helium gas *Superconductors in the Power Grid* (Amsterdam: Elsevier) pp 225–60
- [35] Mason P D *et al* 2015 Scalable design for a high energy cryogenic gas cooled diode pumped laser amplifier *Appl. Opt.* **54** 4227
- [36] Plachta D, Stephens J, Johnson W and Zagarola M 2018 NASA cryocooler technology developments and goals to achieve zero boil-off and to liquefy cryogenic propellants for space exploration *Cryogenics* **94** 95–102